
Neural Implicit Manifold Learning for Topology-Aware Generative Modelling

Brendan Leigh Ross

Layer 6 AI
brendan@layer6.ai

Gabriel Loaiza-Ganem

Layer 6 AI
gabriel@layer6.ai

Anthony L. Caterini

Layer 6 AI
anthony@layer6.ai

Jesse C. Cresswell

Layer 6 AI
jesse@layer6.ai

Abstract

Natural data observed in \mathbb{R}^n is often constrained to an m -dimensional manifold \mathcal{M} , where $m < n$. Current generative models represent this manifold by mapping an m -dimensional latent variable through a neural network $f_\theta : \mathbb{R}^m \rightarrow \mathbb{R}^n$. Such procedures, which we call *pushforward models*, incur a straightforward limitation: manifolds cannot in general be represented with a single parameterization, meaning that attempts to do so will incur either computational instability or the inability to learn probability densities within the manifold. To remedy this problem, we propose to model \mathcal{M} as a *neural implicit manifold*: the set of zeros of a neural network. To learn the data distribution within \mathcal{M} , we introduce *constrained energy-based models*, which use a constrained variant of Langevin dynamics to train and sample within a learned manifold. The resulting model can be manipulated with an *arithmetic of manifolds* which allows practitioners to take unions and intersections of model manifolds. In experiments on synthetic and natural data, we show that constrained EBMs can learn manifold-supported distributions with complex topologies more accurately than pushforward models.

1 Introduction

Generative modelling is the task of estimating an unknown probability distribution P^* using a set of datapoints $\{x_i\} \subset \mathbb{R}^n$ sampled from P^* . Commonly, the distribution of interest lies on an m -dimensional Riemannian submanifold \mathcal{M} embedded in the ambient space \mathbb{R}^n , with $m < n$. For example, the manifold hypothesis states that real-world high-dimensional data tends to have low-dimensional submanifold structure [5]. Elsewhere, data from engineering or the natural sciences can be manifold-supported due to smooth physical constraints [7, 9, 53]. In general, the underlying submanifold \mathcal{M} is unknown *a priori*, which calls for us to design generative models which learn \mathcal{M} in the process of learning P^* .

Initially, one might hope that a sufficiently flexible high-dimensional density estimator trained via maximum likelihood would recover a useful approximation of P^* . However, when modelling data on lower-dimensional manifolds, such methods suffer from *manifold overfitting*, in which fitted models can completely fail to capture the correct density even while maximizing both train and test likelihoods [20, 51]. The typical cure for this dimensionality mismatch is a *pushforward model*: a neural parameterization $f_\theta : \mathbb{R}^m \rightarrow \mathbb{R}^n$ which is trained to transform a low-dimensional prior into a flexible distribution on the data manifold embedded in \mathbb{R}^n (e.g. [2, 3, 73, 80]).

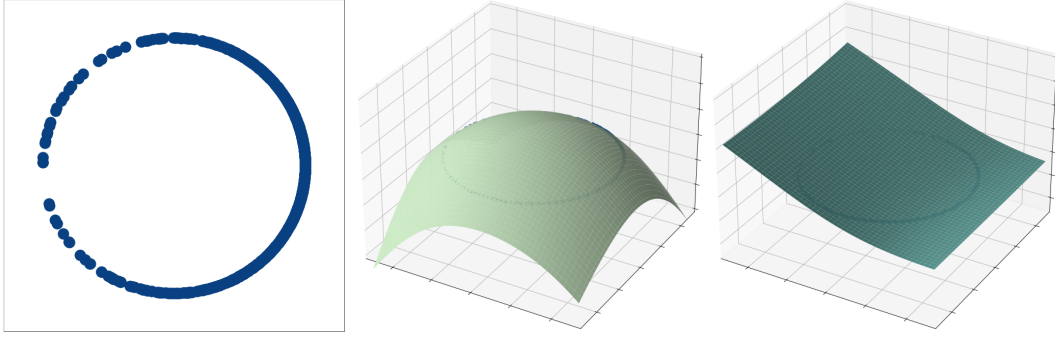


Figure 1: Depiction of our method on simulated circular data from a von Mises distribution. Top row left to right: ground truth sample of von Mises data, a manifold-defining function F_θ learned from the data, and an ambient energy E_ψ trained with constrained Langevin dynamics on the learned manifold. The energy takes the lowest values in areas of high density, precisely as one would expect. The resulting model, defined in Section 3.2, is depicted in the right-hand panel of Figure 2.



Figure 2: Manifold learning and density estimation results on von Mises-distributed data. From left to right: the ground truth, a typical pushforward energy-based model, and a constrained energy-based model (ours). By defining the manifold with a trainable set of constraints $F_\theta(x) = 0$, our method can model distributions with non-trivial topologies.

Modelling a manifold as the image of a single mapping f_θ , however, is topologically restrictive. For example, many approaches encourage an encoder g_ϕ and decoder f_θ to mutually invert each other at each datapoint (e.g. [9, 24, 27, 84]), an objective we can precisely reinterpret as training f_θ to become a diffeomorphism between \mathcal{M} and a subset of the latent space \mathbb{R}^m . This specification conflicts with the fact that, in general, \mathcal{M} may have a complex topology which is not diffeomorphic to any such subset, exposing f_θ to a frontier of tradeoffs between expressivity and numerical stability [4, 18]. Even when f_θ is not a diffeomorphism, its continuity dictates many topological properties of the model manifold, such as connectivity and the number of holes [60].

In this paper we learn data manifolds with a much broader class of topologies using a novel approach outlined in Figure 1. We first learn a manifold *implicitly* as the zero set of a neural network F_θ , controlling the manifold dimension by regularizing the rank of its Jacobian. We then model the density within the manifold using a *constrained energy-based model* E_ψ , which uses constrained Langevin dynamics to sample points on the learned manifold. We show that constrained energy-based models on manifolds maintain the compositionality property of standard energy-based models [40]; manifold-defining functions F_θ along with their energies E_ψ can be combined to take unions and intersections of data manifolds in what we call *manifold arithmetic*. We demonstrate theoretically and empirically that the proposed model can learn manifold-supported distributions more accurately than the pushforward paradigm prevalent in the current literature.

2 Background and related work

2.1 Modelling manifold-supported data

Manifold structure As above, suppose $\{x_i\}$ is a set of samples drawn from probability measure P^* whose support is $\mathcal{M} \subset \mathbb{R}^n$, an m -dimensional Riemannian submanifold of n -dimensional Euclidean space. We focus on the case where $m < n$, so that \mathcal{M} is “infinitely thin” in \mathbb{R}^n , meaning P^* does not admit a probability density with respect to the standard Lebesgue measure. However, we may assume it has a density $p^*(x)$ with respect to the Riemannian measure of \mathcal{M} . We elaborate on this setup in Appendix A.1.

Models for manifold-supported data have long been of interest in statistics, machine learning, and various applications [22, 56]. A common theme in machine learning has been to account for or attribute performance to underlying manifold structure in data [5, 63, 71]. In particular, a number of past works have explored Monte Carlo methods on manifolds [10, 13, 87], which we put to use here. However, the problem of simultaneously learning a submanifold *and* an underlying density has only become of interest in tandem with recent advances in deep generative modelling [9]. To our knowledge, all such models fall under the umbrella of *pushforward models*.

Density estimation with pushforward models When manifold-supported, P^* is most commonly modelled as the *pushforward* of some latent distribution:

$$z \sim p_\psi(z), \quad x = f_\theta(z), \quad (1)$$

where $f_\theta : \mathbb{R}^m \rightarrow \mathbb{R}^n$ is a smooth mapping given by a neural network and $z \sim p_\psi(z)$ is a (possibly trainable) prior on m -dimensional latent space. The resulting model distribution $P_{\theta,\psi}$ is supported on the model manifold¹ $\mathcal{M}_\theta := f_\theta(\mathbb{R}^m)$. This framework encompasses generative adversarial networks (GANs) [3, 32], injective flows [9, 16, 74], and various regularized autoencoders [30, 48, 52, 80]. Since we take the support to be an m -dimensional submanifold, we rule out bijective normalizing flows [23, 69] and variational autoencoders (VAEs) [46], unless $p_\theta(x|z)$ is a point mass.

In recent work, Loaiza-Ganem et al. [51] outline a general procedure for density estimation on manifolds with pushforward models, which separates modelling into two components: a *generalized autoencoder*, which embeds the data manifold into m -dimensional latent space, and a *density estimator*, which learns the density within the manifold. The generalized autoencoding step treats f_θ as a decoder, pairing it with a smooth encoder $g_\phi : \mathbb{R}^n \rightarrow \mathbb{R}^m$, and trains them to learn \mathcal{M} by mutually inverting each other on the data,² such as by minimizing a reconstruction loss $\mathbb{E}_{x \sim P^*} \|x - f_\theta(g_\phi(x))\|^2$. The density estimator $p_\psi(z)$ is then fitted to the encoded data $\{g_\phi(x_i)\}$ via maximum-likelihood. Given a datapoint $x \in \mathcal{M}$, two-step models yield the following estimate for the ground truth density $p^*(x)$:

$$p_{\theta,\psi}(x) = p_\psi(z) |\det J_{f_\theta}^\top(z) J_{f_\theta}(z)|^{-1/2}, \quad (2)$$

where $z := g_\phi(x)$ is the encoding of x and J_{f_θ} is the Jacobian of f_θ with respect to its inputs z . The fidelity of this estimate depends on the condition $f_\theta(g_\phi(x)) = x$ for all $x \in \mathcal{M}$; in other words, g_ϕ must be a right-inverse of f_θ on \mathcal{M} . Injective flow models [9, 16, 47, 74] enforce invertibility on \mathcal{M}_θ with architectural constraints; other two-step models [30, 73, 84], like Loaiza-Ganem et al. [51], achieve this condition at their non-parametric optimum.

Topological challenges Despite the broad applicability of this density estimation procedure, the requisite right-invertibility condition is *effectively impossible* to satisfy for general manifolds \mathcal{M} . If $f_\theta(g_\phi(x)) = x$ for all $x \in \mathcal{M}$, then by definition, g_ϕ smoothly embeds³ \mathcal{M} into \mathbb{R}^m . This condition presents an immediate topological challenge: \mathcal{M} is an m -dimensional manifold, which in general cannot be embedded in m -dimensional Euclidean space. In line with the *strong Whitney embedding*

¹ \mathcal{M} may not formally be a manifold if f_θ is not an embedding because the resulting image can “self-intersect,” but this distinction can be ignored in practice for density estimation models, as we will soon justify.

²In particular, f_θ becomes a left inverse of g_ϕ , and equivalently, g_ϕ becomes a right inverse of f_θ .

³Here we use the word “embed” in the strict topological sense. In machine learning, “embed” can refer more loosely to the creation of a lossy representation of high-dimensional data, but generalized autoencoders attempt to construct a lossless representation in line with the topological meaning.

theorem [50, pg.135], \mathcal{M} might not be embeddable in Euclidean space of less than $2m$ dimensions.⁴ It is thus impossible in the general case for the support of the prior $p_\psi(z)$ to match \mathcal{M} topologically; see the middle panel of Figure 2 for an example.

In the presence of this topological mismatch, one might hope that \mathcal{M}_θ can sufficiently approximate \mathcal{M} with enough capacity and training. However, Cornish et al. [18] show that when this is possible, the bi-Lipschitz constant of f_θ will diverge to infinity, rendering f_θ either analytically non-injective or numerically unstable, making density estimates unreliable [4]. Accordingly, the topological woes of pushforward models cannot be “brute-forced” into submission.

Awareness of the data manifold’s topology may be necessary for downstream applications such as defending against adversarial examples [43] or out-of-distribution detection [15]. In the injective normalizing flows literature in particular, there has been interest in learning manifolds with multiple charts [44, 76], which are certainly more expressive than using a single chart. Thus far, such approaches require ancillary models for inference, which can complicate density estimation, and must set the number of charts as a hyperparameter. Multiple charts also may not be guaranteed to overlap perfectly, misspecifying the manifold.

2.2 Implicitly defined manifolds

The aforementioned limitations of pushforward models stem from the inability of smooth embeddings of \mathbb{R}^m to characterize anything but the simplest of manifolds. A richer class of manifolds can be defined *implicitly*, as given by the following fact from differential geometry [50, pg.105]:

The full-rank zero set theorem Let $U \subseteq \mathbb{R}^n$ be an open subset of \mathbb{R}^n , and let $F : U \rightarrow \mathbb{R}^{n-m}$ be a smooth map. If the Jacobian matrix J_F of F has full rank on its zero set $F^{-1}(\{0\}) := \{x \in U : F(x) = 0\}$, then $F^{-1}(\{0\})$ is a properly embedded submanifold of dimension m in \mathbb{R}^n .

In this paper, we exploit this theorem by constructing a neural network F_θ and defining a new model manifold $\mathcal{M}_\theta := F_\theta^{-1}(\{0\})$. We call F_θ the *manifold-defining function* (MDF) of \mathcal{M}_θ . In the context of 3D shape modelling, related methods have been used with great success [17, 35, 61]. Here we target probabilistic modelling and propose a necessarily more tractable way to fit F_θ to data manifolds of any dimension m embedded in any dimension n . We refer to such manifolds as *implicitly defined* or *implicit*. These are not to be confused with the unrelated term *implicit generative model*, which has been used to describe both energy-based models [25] and some types of pushforward models [59].

2.3 Energy-based models

Energy-based models (EBMs) have a long history in machine learning [49] and even longer in physics [31], but Du and Mordatch [25] introduced the first deep EBM for generative modelling. Notably, they use Langevin dynamics [82], a continuous MCMC algorithm, to generate samples. Training strategies and applications for EBMs have since become popular in the literature [33, 34]. Xiao et al. [85] and Arbel et al. [2] model EBMs in the latent spaces of VAEs and GANs, respectively, yielding EBM-based pushforward models. Arbel et al. [2] in particular show that their method is equivalent to constraining an EBM to the image of their generator, while our approach constrains an EBM to an implicit manifold.

3 Method

3.1 Neural implicit manifolds

Let $F_\theta : \mathbb{R}^n \rightarrow \mathbb{R}^{n-m}$ be a smooth neural network with parameters θ ; our goal is to optimize it to become a manifold-defining function for \mathcal{M} , the data manifold. F_θ thus needs to meet two conditions:

1. $F_\theta(x) = 0$ for all $x \in \mathcal{M}$.
2. $J_{F_\theta}(x)$ has full rank for all $x \in \mathcal{M}$.

⁴A naive solution would be to increase the model’s latent space dimensionality to $2m$; however, this would make the encoded data $\{g_\phi(x_i)\}$ singular in \mathbb{R}^{2m} , invalidating density estimates.

Since \mathcal{M} is the support of P^* , condition 1 is encouraged by optimizing toward the constraint $\mathbb{E}_{x \sim P^*} \|F_\theta(x)\| = 0$, which we achieve by minimizing $\mathbb{E}_{x \sim P^*} \|F_\theta(x)\|^2$.

To achieve condition 2 when modelling surfaces in 3D space, past literature has bounded the L_2 norm of the gradient J_{F_θ} away from zero [35]. However, this does not generalize to any number of dimensions. Null singular values can still be present when, for example, the Frobenius norm or the operator norm of J_{F_θ} is bounded away from zero. To maintain full rank, we need to bound *all* singular values away from zero, for which we take inspiration from Kumar et al. [48]. Given their decoder f_θ , they seek to make the Jacobian $J_{f_\theta}(z)$ *injective* by bounding $\|J_{f_\theta}(z)u\|$ away from zero for all unit-norm vectors $u \in \mathbb{R}^m$. We can do the same, except by bounding $\|v^T J_{F_\theta}(x)\|$ away from zero for all unit-norm $v \in \mathbb{R}^{n-m}$, since we seek to make $J_{F_\theta}(x)$ *surjective*.⁵

Combining these together, we propose the following loss:

$$\mathcal{L}(\theta) = \mathbb{E}_{x \sim P^*, v \sim \text{Unif}(S)} \left[\|F_\theta(x)\|^2 + \alpha (\eta - \|v^T J_{F_\theta}(x)\|)_+^2 \right], \quad (3)$$

where $\text{Unif}(S)$ is the uniform distribution on the unit sphere $S := \{x \in \mathbb{R}^{n-m} : \|x\| = 1\}$, $(\cdot)_+$ is the ReLU function, and α and η are hyperparameters determining the weight of the rank-regularization term and the minimum singular value of J_{F_θ} , respectively. Empirically speaking, the Jacobian regularization term obviates degeneracy in the MDF. Even if we enforce analytical surjectivity in the Jacobian by structuring F_θ as the left-inverse of an injective flow [47], F_θ can still converge towards degeneracy without regularization (Figure 3).

Expressivity Making the simplifying assumption that neural networks can embody any smooth function [19, 41], we may compare the expressivity of neural implicit manifold models with pushforward manifold models. Pushforward models can model densities on precisely those manifolds which are diffeomorphic to a subset of \mathbb{R}^m .

On the other hand, a broader class of manifolds can be modelled as a neural implicit manifold. \mathcal{M} can be represented implicitly if and only if it satisfies the technical condition that its normal bundle is “trivial” [50, pg.271]. Non-trivial normal bundles are not commonly seen in low-dimensional examples except in non-orientable manifolds such as the Möbius strip or Klein bottle. Though it is unclear whether the manifolds of most natural datasets have trivial normal bundles (Carlsson et al. [14] for example find a dataset of image patches to have the topology of a Klein bottle), it is certainly a much broader class than what pushforward models can capture.

Manifold arithmetic Some datasets might satisfy multiple constraints, which one might want to learn separately before combining into a mixture or product of models. Since implicit manifold learning can be interpreted as learning a set of constraints, neural implicit manifolds exhibit composability similar to energy-based models [40, 58]. If F_1 and F_2 are MDFs for \mathcal{M}_1 and \mathcal{M}_2 respectively, then the union $\mathcal{M}_1 \cup \mathcal{M}_2$ is the zero set of the product of functions $x \mapsto F_1(x)F_2(x)$. Concatenating outputs into the function $x \mapsto (F_1(x), F_2(x))$ instead produces the intersection $\mathcal{M}_1 \cap \mathcal{M}_2$. We note that $\mathcal{M}_1 \cup \mathcal{M}_2$ and $\mathcal{M}_1 \cap \mathcal{M}_2$ need not be manifolds anymore, meaning we can combine MDFs to form complex structures that cannot be described with a single manifold. Taking intersections and unions could, for example, be used to model conjunctions or disjunctions of data labelled with multiple overlapping attributes [26].

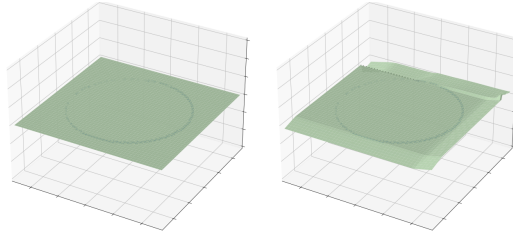


Figure 3: Manifold defining functions F_θ trained without regularizing J_{F_θ} . The first is a regular neural network which has become completely flat; $F^{-1}(\{0\})$ is the entire space. The second is the left-inverse of an injective flow, whose Jacobian has full rank analytically. However, it can become arbitrarily close to being flat, meaning it can send $\mathbb{E}_{x \sim P^*} \|F_\theta(x)\|^2 \rightarrow 0$ without learning the manifold. These should be contrasted to the second pane of Figure 1.

⁵Note we are here referring to a matrix as injective (resp. surjective) if it has full column (resp. row) rank.

3.2 Constrained energy-based modelling

In this section we introduce the *constrained energy-based model* for density estimation on implicit manifolds \mathcal{M}_θ . Let $E_\psi : \mathbb{R}^n \rightarrow \mathbb{R}$ be an energy function represented by a neural network and define the corresponding density as follows:

$$p_{\theta,\psi}(x) = \frac{e^{-E_\psi(x)}}{\int_{\mathcal{M}_\theta} e^{-E_\psi(y)} dy}, \quad x \in \mathcal{M}_\theta, \quad (4)$$

where dy can be equivalently thought of as the Riemannian volume form or Riemannian measure of \mathcal{M}_θ (see Appendix A.1 for details). Let $P_{\theta,\psi}$ be the resulting probability measure (we can think of $P_{\theta,\psi}$ as a probability distribution characterized by both the manifold \mathcal{M}_θ and the density $p_{\theta,\psi}$). Since the energy E_ψ is defined on the full ambient space \mathbb{R}^n but the corresponding model is defined only from its values on \mathcal{M}_θ , we refer to $P_{\theta,\psi}$ as a *constrained energy-based model*.

Having defined $p_{\theta,\psi}$ and fixed the manifold \mathcal{M}_θ , we seek to maximize log-likelihood on the data via gradient-based optimization of E_ψ . Since the denominator $\int_{\mathcal{M}_\theta} e^{-E_\psi(y)} dy$ is in general an intractable integral, we resort to contrastive divergence [40]:

$$\nabla_\psi \log p_{\theta,\psi}(x_i) = -\nabla_\psi E_\psi(x_i) + \mathbb{E}_{x \sim P_{\theta,\psi}} [\nabla_\psi E_\psi(x)]. \quad (5)$$

Importantly, the right-most term in Equation 5 is an expectation taken over $P_{\theta,\psi}$, so samples from the model are required for optimization.

Constrained Langevin Monte Carlo How can one sample from $P_{\theta,\psi}$? Du and Mordatch [25] use Langevin dynamics, a continuous MCMC method, to sample from deep EBMs. For constrained EBMs, standard Langevin dynamics is insufficient, as it will produce off-manifold samples from the energy. We need a manifold-aware MCMC method.

One such method is constrained Hamiltonian Monte Carlo (CHMC), a family of Markov chain Monte Carlo models for implicitly defined manifolds proposed by Brubaker et al. [10]. Our main contribution in this section, aside from defining constrained EBMs, is to show that CHMC, which is typically applied to analytically known manifolds, can be adapted to manifolds implicitly defined by neural networks. In particular, we show how to avoid the memory-prohibitive operation of explicitly constructing the Jacobian of F_θ , which features prominently in CHMC.

We focus on the special case of constrained Langevin Monte Carlo. Fixing a step size ε and suppressing parameter subscripts for brevity, a single iteration from position $x^{(t)}$ to $x^{(t+1)}$ requires two steps:

1. Sample a momentum $r \sim N(0, I_n)$ conditioned on membership of the tangent space of \mathcal{M} at $x^{(t)}$. This can be done by sampling $r' \sim N(0, I_n)$ and projecting onto the null space of $J_F(x^{(t)})$ (written as J_F for clarity):

$$r := r' - J_F^T (J_F J_F^T)^{-1} J_F r'. \quad (6)$$

2. Solve for the new position $x^{(t+1)}$ using a constrained Leapfrog step, which entails solving the following system of equations for $x^{(t+1)}$ and the Lagrange multiplier $\lambda \in \mathbb{R}^{n-m}$:

$$x^{(t+1)} = x^{(t)} + \varepsilon r - \frac{\varepsilon^2}{2} \nabla_x E(x^{(t)}) - \frac{\varepsilon^2}{2} J_F(x^{(t)})^T \lambda \quad (7)$$

$$F(x^{(t+1)}) = 0. \quad (8)$$

Now we describe how Equations 6 and 7 can be computed without constructing J_{F_θ} . With access to efficient Jacobian-vector product and vector-Jacobian product routines, such as those available in functorch [36], any expression in the form of $J_F w$ for $w \in \mathbb{R}^n$ or $J_F^T v = (v^T J_F)^T$ for $v \in \mathbb{R}^{n-m}$ is tractable. Furthermore, the inverse term on the right-hand side of Equation 6 can be computed with inspiration from work in injective flows by Caterini et al. [16] who overcome a similar expression using the conjugate gradients (CG) routine [28, 62, 67] and their *forward-backward auto-differentiation trick*. CG allows us to compute expressions of the form $A^{-1}b$, where A is an $(n-m) \times (n-m)$ matrix. In particular, CG requires access only to the operation $v \mapsto Av$, not the matrix A itself. In our case, $b = J_F r'$, a Jacobian-vector product, and the operation is $v \mapsto J_F J_F^T v$,

which is again computable as a vector-Jacobian product followed by a Jacobian-vector product. Due to the shape of J_F , this operation is most efficiently performed using backward followed by forward-mode auto-differentiation, so our method can be termed the *backward-forward* variant.

Equations 7 and 8 can be combined into a single minimization problem which can be easily optimized by second-order methods such as L-BFGS [12]:

$$\lambda^* = \operatorname{argmin}_{\lambda} \left\| F_{\theta} \left(x^{(t)} + \varepsilon r - \frac{\varepsilon^2}{2} \nabla_x E_{\psi}(x^{(t)}) - \frac{\varepsilon^2}{2} J_{F_{\theta}}(x^{(t)})^T \lambda \right) \right\|, \quad (9)$$

where, in computationally challenging contexts, we can settle for suboptimal solutions at the cost of introducing some bias. We note that L-BFGS outperformed first-order methods like stochastic gradient descent [72] or Adam [45] for optimization arguments of this size. Once obtained, λ^* can be plugged back into Equation 7 to directly calculate $x^{(t+1)}$.

The two steps described above constitute a single iteration of constrained Langevin dynamics. In practice, many iterations are required to obtain a good approximation to sampling from $P_{\theta, \psi}$. Constrained Langevin Monte Carlo is summarized in full in Algorithm 1. Following Du and Mordatch [25], we use a sample buffer for 95% of generated samples to assist convergence during training. To obtain completely new samples, we sample random noise in ambient space and project them to \mathcal{M}_{θ} by computing $\operatorname{argmin}_x \|F_{\theta}(x)\|^2$ with L-BFGS.

Algorithm 1 Constrained Langevin Monte Carlo

Require: manifold-defining function F_{θ} , energy E_{ψ} , step size ε , step count k , initial point x_0

```

 $x \leftarrow x_0$ 
for  $t = 1, \dots, k$  do
   $r' \sim N(0, I_n)$ 
   $r \leftarrow r' - J_{F_{\theta}}^T (J_{F_{\theta}} J_{F_{\theta}}^T)^{-1} J_{F_{\theta}} r'$ 
   $\lambda^* \leftarrow \operatorname{argmin}_{\lambda} \left\| F_{\theta} \left( x + \varepsilon r - \frac{\varepsilon^2}{2} \nabla_x E_{\psi}(x) - \frac{\varepsilon^2}{2} J_{F_{\theta}}(x)^T \lambda \right) \right\|$ 
   $x \leftarrow x + \varepsilon r - \frac{\varepsilon^2}{2} \nabla_x E_{\psi}(x) - \frac{\varepsilon^2}{2} J_{F_{\theta}}(x)^T \lambda^*$ 
end for
return  $x$ 

```

4 Experiments

Constrained energy-based models on neural implicit manifolds represent a novel method which we hope can be scaled up in the future to datasets with high-dimensional manifold structure such as images. For this experiment section, we note that density estimation on manifolds even of few dimensions is of interest in the literature [21, 29, 54, 70]. Such models are typically bespoke: constructed using known geometric properties of the manifold.

Here we show that constrained EBMs are the best choice for such distributions in the absence of *a priori* knowledge of the manifold. We reiterate that all manifolds learned in these experiments are determined only based on samples, without any additional knowledge. Quantitative comparisons of density estimates are challenging when manifolds are unknown: densities on different learned manifolds have different base measures, so likelihood values are incomparable. For image data, comparisons are made on the basis of proxies such as the Fréchet inception distance [38], which is not available for non-image data. Fortunately, we can visualize the following datasets to verify performance qualitatively.

As discussed in Section 2, the class of pushforward density estimation models is large, and any can serve as a basis of comparison. We focus on the most comparable baseline: a simple pushforward EBM consisting of an autoencoder with an EBM in the latent space. We experimented with replacing the normal autoencoder objective with a Gaussian VAE objective in pursuit of stable latent representations, but found that in order to learn the manifold, the KL-divergence term had to be downweighted to the point that results were no different from a regular autoencoder.

Our code is written in PyTorch [64]. We use GPyTorch [28] to compute conjugate gradients and the marching cubes algorithm of Yatagawa [86] to plot 2D implicit manifolds embedded in 3D. We

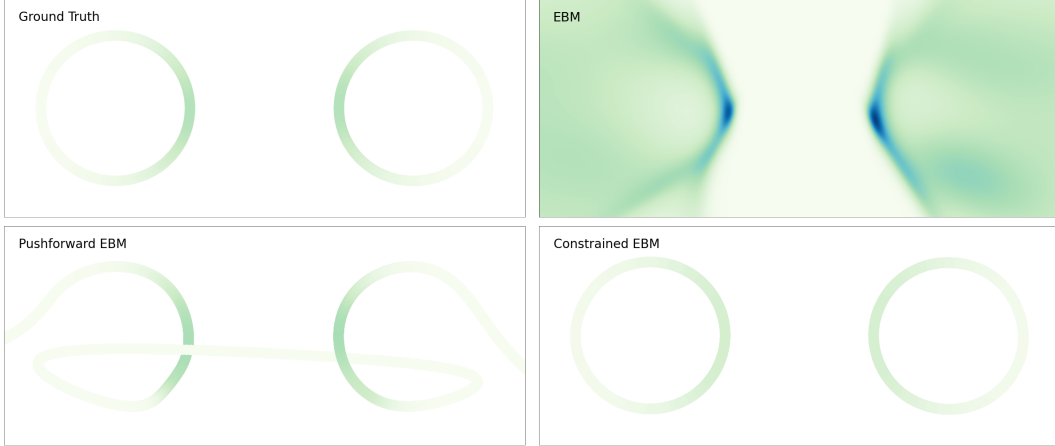


Figure 4: Manifold learning and density estimation results on a balanced, disjoint mixture of two von Mises distributions. Four models are depicted: the ground truth, an ambient EBM, a pushforward EBM, and a constrained EBM (ours).

generate synthetic data with Pyro [6]. Hyperparameter settings and other details can be found in Appendix A.2.

4.1 Synthetic data

Density estimation In our first experiment, we evaluate density estimation ability on 1000 points sampled from a mixture of two von Mises distributions on circles embedded in 2D. Results for an ordinary EBM, a pushforward EBM, and a constrained EBM are visible in Figure 4. Of note is the topology of the density learned by the pushforward EBM; it is necessarily connected and appears to be diffeomorphic to the real line except at two points of self-intersection. The constrained EBM, in contrast, captures the manifold even in regions of sparsity. The ordinary EBM is not subject to the *topological* limitations of the pushforward EBM, but it still lacks the inductive bias to learn the low intrinsic dimension of the data, except perhaps on the insides of the circles.

Manifold arithmetic In this experiment, we highlight the ability of constrained EBMs to perform manifold arithmetic. Practical applications of this capability are left to future research. Figure 5 depicts two modes of composition for constrained EBMs. The constrained EBM depicted on the left is learned from 1000 points sampled from a balanced mixture of two projected normal distributions: the distribution given by sampling from a normally distributed random variable and projecting to the unit sphere. After this, with no additional training to our model, we manipulate it to create new probability models. First, two copies of the learned model are translated by 0.5 units in opposite directions along the x -axis.

- A new model given by the union of these two copies is depicted in the middle pane of Figure 5: it consists of the product of their MDFs and a balanced mixture of their corresponding energies. Note that the new surface self-intersects, and is no longer formally an embedded submanifold.
- Another new model given by the intersection of these two copies is visible in the final pane. By concatenating the output of the MDFs and summing the corresponding energies, we arrive at a circle embedded in three dimensions.

4.2 Natural data

Geospatial data Following Mathieu and Nickel [54], we model a dataset of global flood events from the Dartmouth Flood Observatory⁶ [8], embedded on a sphere representing the Earth. Despite

⁶The Dartmouth Flood Observatory’s global active archive is available without charge for research and education purposes.

the relative sparsity of floods compared to previous datasets (they do not occur on water), the constrained EBM still perfectly learns the spherical shape of the Earth. The pushforward EBM, while representing the densities fairly well, struggles to learn the sphere, and places some density off of the true manifold. Note that the constrained and pushforward EBMs are plotted using a triangular mesh and mesh grid, respectively, due to the difference in how they are defined.

Amino acid modelling The structure of amino acids can be characterized by a pair of dihedral angles and thus possesses toroidal geometry. Designing flexible probabilistic models for torus-supported data is consequently of interest in the bioinformatics literature on protein structure prediction [1, 53, 77], and so amino acid angle data is a practical candidate for evaluating the density estimation ability of constrained EBMs. In Figure 7, we compare a constrained EBM against a pushforward EBM using an open-source amino acid dataset available from the NumPyro software package [66]. Remarkably, although we do experience failure cases (Appendix A.2), our manifold-defining function learns the torus well in the presence of sparse data. We postulate that our training procedure imparts an inductive bias towards learning closed manifolds. On the other hand, the pushforward EBM was unable to reliably model the manifolds. This drop in performance is concerning because high-dimensional datasets, to which pushforward models are often applied, are expected to have complex topologies. We hope that some of the improvements observed for constrained EBMs can be extended to other domains in the future.

5 Conclusion

In this paper we observed that all existing techniques to jointly learn data manifolds and densities can be described as *pushforward models*. These models must become near-diffeomorphisms, an overly strong topological limitation, in order to provide reliable density estimates. To avoid this limitation, we proposed to learn the data manifold *implicitly* with a neural network F_θ . We then proposed the *constrained EBM*, a new type of EBM for modelling data on neural implicit manifolds. In both cases, we showed how any computational difficulty due to the Jacobian of F_θ can be “tamed” using stochastic estimates and automatic differentiation tricks inspired by the injective flows literature [16, 48] which frequently grapples with non-square Jacobians. Finally, we showed the qualitative efficacy of constrained EBMs on both synthetic and real-world tasks.

Although we have covered the limitations of pushforward models when used for density estimation, we highlight here some of their advantages over our model. Primarily, pushforward models come with latent representations of data, which can be used for image manipulation [83], explainability and artificial reasoning [39, 55], and efficient density estimation in the latent space. A promising direction for future work is to combine these benefits with those of constrained EBMs.

Our model inherits all the difficulties of training EBMs; for example, it relies on the assumption of convergence of Langevin dynamics, which occurs only with infinite steps. Sampling remains slower than normal EBMs due to the complexity of constrained Langevin dynamics steps. Constrained

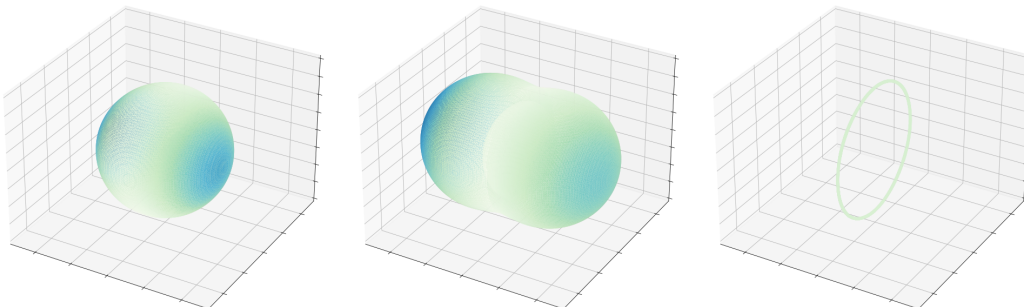


Figure 5: Performing manifold arithmetic using an implicitly learned sphere. From left to right: a spherical distribution learned by a constrained EBM, a new model given by the union of two copies of the same model translated in different directions, and a new model given by the intersection of the same two copies.

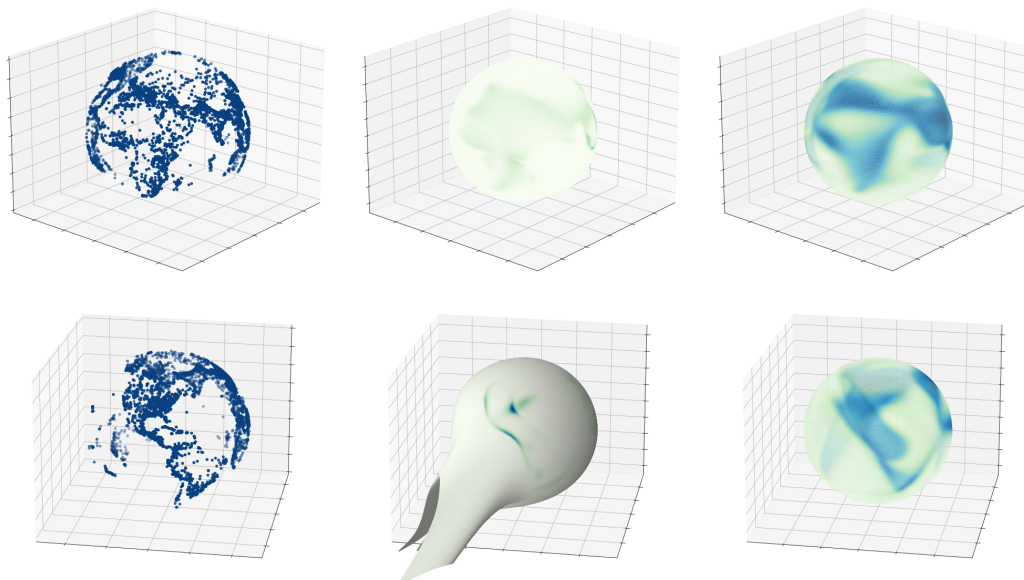


Figure 6: Manifold learning and density estimation results on flood location data. From left to right with two different viewpoints (top and bottom): the ground truth data, a pushforward EBM, and a constrained EBM.

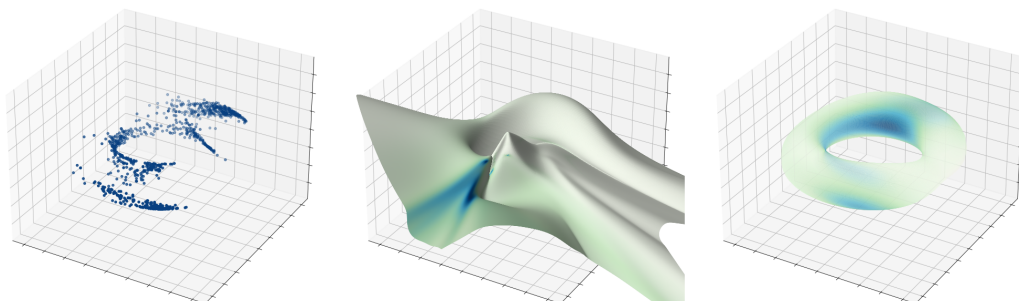


Figure 7: Manifold learning and density estimation results on the glycine angle data. From left to right: the ground truth data, a pushforward EBM, and a constrained EBM.

EBMs might thus be better scaled by training methods that do not require sampling, such as learning the Stein discrepancy [34] or score-based techniques [21, 78].

Generative models can be used maliciously [11, 81] and can inherit biases from their data [79]. If constrained EBMs or any follow-up work are scaled to high-dimensional data such as images, they can lead to harmful practices, such as the deceptive application of deepfakes [57]. However, learning the data manifold correctly may enable fairer and more explainable outcomes, for example by decreasing gender bias [42].

Acknowledgments and Disclosure of Funding

The authors declare no additional funding sources or competing interests.

References

- [1] J. Ameijeiras-Alonso and C. Ley. Sine-skewed toroidal distributions and their application in protein bioinformatics. *arXiv preprint arXiv:1910.13293*, 2019.

- [2] M. Arbel, L. Zhou, and A. Gretton. Generalized Energy Based Models. In *International Conference on Learning Representations*, 2021.
- [3] M. Arjovsky, S. Chintala, and L. Bottou. Wasserstein Generative Adversarial Networks. In *Proceedings of the 34th International Conference on Machine Learning*, volume 70, pages 214–223, 06–11 Aug 2017.
- [4] J. Behrmann, P. Vicol, K.-C. Wang, R. Grosse, and J.-H. Jacobsen. Understanding and mitigating exploding inverses in invertible neural networks. In *International Conference on Artificial Intelligence and Statistics*, pages 1792–1800. PMLR, 2021.
- [5] Y. Bengio, A. Courville, and P. Vincent. Representation learning: A review and new perspectives. *IEEE transactions on pattern analysis and machine intelligence*, 35(8):1798–1828, 2013.
- [6] E. Bingham, J. P. Chen, M. Jankowiak, F. Obermeyer, N. Pradhan, T. Karaletsos, R. Singh, P. A. Szerlip, P. Horsfall, and N. D. Goodman. Pyro: Deep universal probabilistic programming. *J. Mach. Learn. Res.*, 20:28:1–28:6, 2019. URL <http://jmlr.org/papers/v20/18-403.html>.
- [7] W. Boomsma, K. V. Mardia, C. C. Taylor, J. Ferkinghoff-Borg, A. Krogh, and T. Hamelryck. A generative, probabilistic model of local protein structure. *Proceedings of the National Academy of Sciences*, 105(26):8932–8937, 2008.
- [8] G. R. Brakenridge. Global active archive of large flood events. *Dartmouth Flood Observatory, University of Colorado*, 2010.
- [9] J. Brehmer and K. Cranmer. Flows for simultaneous manifold learning and density estimation. In *Advances in Neural Information Processing Systems*, volume 33, 2020.
- [10] M. Brubaker, M. Salzmann, and R. Urtasun. A Family of MCMC Methods on Implicitly Defined Manifolds. In *Proceedings of the Fifteenth International Conference on Artificial Intelligence and Statistics*, volume 22, pages 161–172, 21–23 Apr 2012.
- [11] M. Brundage, S. Avin, J. Clark, H. Toner, P. Eckersley, B. Garfinkel, A. Dafoe, P. Scharre, T. Zeitzoff, B. Filar, H. Anderson, H. Roff, G. C. Allen, J. Steinhardt, C. Flynn, S. O. hÉigeartaigh, S. Beard, H. Belfield, S. Farquhar, C. Lyle, R. Crootof, O. Evans, M. Page, J. Bryson, R. Yampolskiy, and D. Amodei. The malicious use of artificial intelligence: Forecasting, prevention, and mitigation. *arXiv:1802.07228*, 2018.
- [12] R. H. Byrd, P. Lu, J. Nocedal, and C. Zhu. A limited memory algorithm for bound constrained optimization. *SIAM Journal on scientific computing*, 16(5):1190–1208, 1995.
- [13] S. Byrne and M. Girolami. Geodesic Monte Carlo on embedded manifolds. *Scandinavian Journal of Statistics*, 40(4):825–845, 2013.
- [14] G. Carlsson, T. Ishkhanov, V. De Silva, and A. Zomorodian. On the local behavior of spaces of natural images. *International journal of computer vision*, 76(1):1–12, 2008.
- [15] A. L. Caterini and G. Loaiza-Ganem. Entropic issues in likelihood-based ood detection. In *I (Still) Can't Believe It's Not Better! Workshop at NeurIPS 2021*, pages 21–26. PMLR, 2022.
- [16] A. L. Caterini, G. Loaiza-Ganem, G. Pleiss, and J. P. Cunningham. Rectangular flows for manifold learning. In *Advances in Neural Information Processing Systems*, volume 34, 2021.
- [17] Z. Chen and H. Zhang. Learning implicit fields for generative shape modeling. In *Proceedings of the IEEE/CVF Conference on Computer Vision and Pattern Recognition*, pages 5939–5948, 2019.
- [18] R. Cornish, A. Caterini, G. Deligiannidis, and A. Doucet. Relaxing bijectivity constraints with continuously indexed normalising flows. In *International Conference on Machine Learning*, pages 2133–2143. PMLR, 2020.
- [19] B. C. Csáji et al. Approximation with artificial neural networks. *Faculty of Sciences, Eötvös Loránd University, Hungary*, 24(48):7, 2001.

- [20] B. Dai and D. Wipf. Diagnosing and Enhancing VAE Models. In *International Conference on Learning Representations*, 2019.
- [21] V. De Bortoli, E. Mathieu, M. Hutchinson, J. Thornton, Y. W. Teh, and A. Doucet. Riemannian score-based generative modeling. *arXiv preprint arXiv:2202.02763*, 2022.
- [22] P. Diaconis, S. Holmes, and M. Shahshahani. Sampling from a manifold. In *Advances in modern statistical theory and applications: a Festschrift in honor of Morris L. Eaton*, pages 102–125. Institute of Mathematical Statistics, 2013.
- [23] L. Dinh, J. Sohl-Dickstein, and S. Bengio. Density estimation using Real NVP. *ICLR*, 2017.
- [24] J. Donahue, P. Krähenbühl, and T. Darrell. Adversarial feature learning. *ICLR*, 2017.
- [25] Y. Du and I. Mordatch. Implicit Generation and Modeling with Energy Based Models. *Advances in Neural Information Processing Systems*, 32:3608–3618, 2019.
- [26] Y. Du, S. Li, and I. Mordatch. Compositional visual generation with energy based models. *Advances in Neural Information Processing Systems*, 33:6637–6647, 2020.
- [27] V. Dumoulin, I. Belghazi, B. Poole, O. Mastropietro, A. Lamb, M. Arjovsky, and A. Courville. Adversarially learned inference. *ICLR*, 2017.
- [28] J. Gardner, G. Pleiss, K. Q. Weinberger, D. Bindel, and A. G. Wilson. Gpytorch: Blackbox matrix-matrix gaussian process inference with gpu acceleration. *Advances in neural information processing systems*, 31, 2018.
- [29] M. C. Gemici, D. Rezende, and S. Mohamed. Normalizing flows on Riemannian manifolds. *arXiv preprint arXiv:1611.02304*, 2016.
- [30] P. Ghosh, M. S. Sajjadi, A. Vergari, M. Black, and B. Schölkopf. From variational to deterministic autoencoders. *ICLR*, 2020.
- [31] J. W. Gibbs. *Elementary principles in statistical mechanics: developed with especial reference to the rational foundations of thermodynamics*. C. Scribner’s sons, 1902.
- [32] I. J. Goodfellow, J. Pouget-Abadie, M. Mirza, B. Xu, D. Warde-Farley, S. Ozair, A. Courville, and Y. Bengio. Generative adversarial nets. In *Proceedings of the 27th International Conference on Neural Information Processing Systems-Volume 2*, pages 2672–2680, 2014.
- [33] W. Grathwohl, K.-C. Wang, J.-H. Jacobsen, D. Duvenaud, M. Norouzi, and K. Swersky. Your classifier is secretly an energy based model and you should treat it like one. *arXiv preprint arXiv:1912.03263*, 2019.
- [34] W. Grathwohl, K.-C. Wang, J.-H. Jacobsen, D. Duvenaud, and R. Zemel. Learning the stein discrepancy for training and evaluating energy-based models without sampling. In *International Conference on Machine Learning*, pages 3732–3747. PMLR, 2020.
- [35] A. Gropp, L. Yariv, N. Haim, M. Atzmon, and Y. Lipman. Implicit geometric regularization for learning shapes. *arXiv preprint arXiv:2002.10099*, 2020.
- [36] H. He and R. Zou. functorch: Jax-like composable function transforms for pytorch. <https://github.com/pytorch/functorch>, 2021.
- [37] D. Hendrycks and K. Gimpel. Gaussian error linear units (gelus). *arXiv preprint arXiv:1606.08415*, 2016.
- [38] M. Heusel, H. Ramsauer, T. Unterthiner, B. Nessler, and S. Hochreiter. GANs Trained by a Two Time-Scale Update Rule Converge to a Local Nash Equilibrium. In *Advances in Neural Information Processing Systems*, volume 30, 2017.
- [39] I. Higgins, L. Matthey, A. Pal, C. Burgess, X. Glorot, M. Botvinick, S. Mohamed, and A. Lerchner. beta-vae: Learning basic visual concepts with a constrained variational framework. 2016.

- [40] G. E. Hinton. Training products of experts by minimizing contrastive divergence. *Neural computation*, 14(8):1771–1800, 2002.
- [41] K. Hornik, M. Stinchcombe, and H. White. Multilayer feedforward networks are universal approximators. *Neural networks*, 2(5):359–366, 1989.
- [42] A. I. Humayun, R. Balestrierio, and R. Baraniuk. Magnet: Uniform sampling from deep generative network manifolds without retraining. *arXiv preprint arXiv:2110.08009*, 2021.
- [43] U. Jang, S. Jha, and S. Jha. On the need for topology-aware generative models for manifold-based defenses. *arXiv preprint arXiv:1909.03334*, 2019.
- [44] D. Kalatzis, J. Z. Ye, J. Wohlert, and S. Hauberg. Multi-chart flows. *arXiv preprint arXiv:2106.03500*, 2021.
- [45] D. P. Kingma and J. Ba. Adam: A method for stochastic optimization. *arXiv preprint arXiv:1412.6980*, 2014.
- [46] D. P. Kingma and M. Welling. Auto-encoding Variational Bayes. *ICLR*, 2014.
- [47] K. Kothari, A. Khorashadizadeh, M. de Hoop, and I. Dokmanić. Trumpets: Injective flows for inference and inverse problems. In *Proceedings of the Thirty-Seventh Conference on Uncertainty in Artificial Intelligence*, volume 161, pages 1269–1278, 2021.
- [48] A. Kumar, B. Poole, and K. Murphy. Regularized autoencoders via relaxed injective probability flow. In *International Conference on Artificial Intelligence and Statistics*, pages 4292–4301. PMLR, 2020.
- [49] Y. LeCun, S. Chopra, R. Hadsell, M. Ranzato, and F. Huang. A tutorial on energy-based learning. *Predicting structured data*, 1(0), 2006.
- [50] J. M. Lee. *Introduction to Smooth Manifolds*. Springer, 2013.
- [51] G. Loaiza-Ganem, B. L. Ross, J. C. Cresswell, and A. L. Caterini. Diagnosing and Fixing Manifold Overfitting in Deep Generative Models, 2022. URL <https://arxiv.org/abs/2204.07172>.
- [52] A. Makhzani, J. Shlens, N. Jaitly, I. Goodfellow, and B. Frey. Adversarial autoencoders. *ICLR*, 2016.
- [53] K. V. Mardia, C. C. Taylor, and G. K. Subramaniam. Protein bioinformatics and mixtures of bivariate von mises distributions for angular data. *Biometrics*, 63(2):505–512, 2007.
- [54] E. Mathieu and M. Nickel. Riemannian Continuous Normalizing Flows. In *Advances in Neural Information Processing Systems*, volume 33, 2020.
- [55] E. Mathieu, T. Rainforth, N. Siddharth, and Y. W. Teh. Disentangling disentanglement in variational autoencoders. In *International Conference on Machine Learning*, pages 4402–4412. PMLR, 2019.
- [56] L. McInnes, J. Healy, and J. Melville. Umap: Uniform manifold approximation and projection for dimension reduction. *arXiv preprint arXiv:1802.03426*, 2018.
- [57] Y. Mirsky and W. Lee. The creation and detection of deepfakes: A survey. *ACM Computing Surveys (CSUR)*, 54(1):1–41, 2021.
- [58] A. Mnih and G. Hinton. Learning nonlinear constraints with contrastive backpropagation. In *Proceedings. 2005 IEEE International Joint Conference on Neural Networks, 2005.*, volume 2, pages 1302–1307. IEEE, 2005.
- [59] S. Mohamed and B. Lakshminarayanan. Learning in implicit generative models. *arXiv preprint arXiv:1610.03483*, 2016.
- [60] J. Munkres. *Topology*. Featured Titles for Topology. Prentice Hall, Incorporated, 2000. ISBN 9780131816299. URL <https://books.google.ca/books?id=XjoZAQAIAAJ>.

- [61] M. Niemeyer and A. Geiger. Giraffe: Representing scenes as compositional generative neural feature fields. In *Proceedings of the IEEE/CVF Conference on Computer Vision and Pattern Recognition*, pages 11453–11464, 2021.
- [62] J. Nocedal and S. Wright. *Numerical optimization*. Springer Science & Business Media, 2006.
- [63] A. Ozakin and A. Gray. Submanifold density estimation. *Advances in Neural Information Processing Systems*, 22, 2009.
- [64] A. Paszke, S. Gross, F. Massa, A. Lerer, J. Bradbury, G. Chanan, T. Killeen, Z. Lin, N. Gimeshain, L. Antiga, A. Desmaison, A. Kopf, E. Yang, Z. DeVito, M. Raison, A. Tejani, S. Chilamkurthy, B. Steiner, L. Fang, J. Bai, and S. Chintala. Pytorch: An imperative style, high-performance deep learning library. In H. Wallach, H. Larochelle, A. Beygelzimer, F. d'Alché-Buc, E. Fox, and R. Garnett, editors, *Advances in Neural Information Processing Systems 32*, pages 8024–8035. Curran Associates, Inc., 2019. URL <http://papers.nips.cc/paper/9015-pytorch-an-imperative-style-high-performance-deep-learning-library.pdf>.
- [65] X. Pennec. Probabilities and statistics on riemannian manifolds: Basic tools for geometric measurements. In *NSIP*, volume 3, pages 194–198. Citeseer, 1999.
- [66] D. Phan, N. Pradhan, and M. Jankowiak. Composable effects for flexible and accelerated probabilistic programming in numpyro. *arXiv preprint arXiv:1912.11554*, 2019.
- [67] A. Potapczynski, L. Wu, D. Biderman, G. Pleiss, and J. P. Cunningham. Bias-free scalable gaussian processes via randomized truncations. *International Conference on Machine Learning*, to appear, 2021.
- [68] P. Ramachandran, B. Zoph, and Q. V. Le. Searching for activation functions. *arXiv preprint arXiv:1710.05941*, 2017.
- [69] D. Rezende and S. Mohamed. Variational inference with normalizing flows. In *International Conference on Machine Learning*, pages 1530–1538. PMLR, 2015.
- [70] D. J. Rezende, G. Papamakarios, S. Racaniere, M. Albergo, G. Kanwar, P. Shanahan, and K. Cranmer. Normalizing flows on tori and spheres. In *International Conference on Machine Learning*, pages 8083–8092. PMLR, 2020.
- [71] S. Rifai, Y. N. Dauphin, P. Vincent, Y. Bengio, and X. Muller. The manifold tangent classifier. *Advances in neural information processing systems*, 24, 2011.
- [72] H. Robbins and S. Monro. A stochastic approximation method. *The annals of mathematical statistics*, pages 400–407, 1951.
- [73] R. Rombach, A. Blattmann, D. Lorenz, P. Esser, and B. Ommer. High-Resolution Image Synthesis with Latent Diffusion Models. *arXiv preprint arXiv:2112.10752*, 2021.
- [74] B. L. Ross and J. C. Cresswell. Tractable Density Estimation on Learned Manifolds with Conformal Embedding Flows. In *Advances in Neural Information Processing Systems*, volume 34, 2021.
- [75] W. Rudin. *Real and Complex Analysis, 3rd Ed.* McGraw-Hill, Inc., USA, 1987. ISBN 0070542341.
- [76] S. Sidheekh, C. B. Dock, T. Jain, R. Balan, and M. K. Singh. Vq-flows: Vector quantized local normalizing flows. *arXiv preprint arXiv:2203.11556*, 2022.
- [77] H. Singh, V. Hnizdo, and E. Demchuk. Probabilistic model for two dependent circular variables. *Biometrika*, 89(3):719–723, 2002.
- [78] Y. Song and D. P. Kingma. How to train your energy-based models. *arXiv preprint arXiv:2101.03288*, 2021.

- [79] R. Steed and A. Caliskan. Image representations learned with unsupervised pre-training contain human-like biases. In *Proceedings of the 2021 ACM Conference on Fairness, Accountability, and Transparency*, pages 701–713, 2021.
- [80] I. Tolstikhin, O. Bousquet, S. Gelly, and B. Schoelkopf. Wasserstein auto-encoders. *ICLR*, 2018.
- [81] F. Urbina, F. Lentzos, C. Invernizzi, and S. Ekins. Dual use of artificial-intelligence-powered drug discovery. *Nature Machine Intelligence*, 4(3):189–191, 2022.
- [82] M. Welling and Y. W. Teh. Bayesian learning via stochastic gradient langevin dynamics. In *Proceedings of the 28th international conference on machine learning (ICML-11)*, pages 681–688. Citeseer, 2011.
- [83] W. Xia, Y. Zhang, Y. Yang, J.-H. Xue, B. Zhou, and M.-H. Yang. Gan inversion: A survey. *arXiv preprint arXiv:2101.05278*, 2021.
- [84] Z. Xiao, Q. Yan, and Y. Amit. Generative latent flow. *arXiv preprint arXiv:1905.10485*, 2019.
- [85] Z. Xiao, K. Kreis, J. Kautz, and A. Vahdat. VAEBM: A symbiosis between variational autoencoders and energy-based models. *arXiv preprint arXiv:2010.00654*, 2020.
- [86] T. Yatagawa. torchmcube: marching cubes for pytorch, 2021. URL <https://github.com/tatsy/torchmcubes>.
- [87] E. Zappa, M. Holmes-Cerfon, and J. Goodman. Monte Carlo on manifolds: sampling densities and integrating functions. *arXiv e-prints*, art. arXiv:1702.08446, Feb. 2017.

A Appendix

A.1 Formal setting

Here we expand on the formal setting in which we seek to perform density estimation.

Geometry Let \mathcal{M} be an m -dimensional Riemannian submanifold of ambient space \mathbb{R}^n where $m < n$. Formally this refers to the pair $(\mathcal{M}, \mathbf{g})$, where $\mathcal{M} \subseteq \mathbb{R}^n$ is a manifold and \mathbf{g} is the Riemannian metric inherited from ambient Euclidean space. In other words, \mathbf{g} is the restriction of the canonical Euclidean metric, which is characterized by the standard dot product between vectors, to vectors which are tangent to \mathcal{M} . The metric \mathbf{g} , which is typically implied, captures the curvature information we would like to associate with \mathcal{M} .

A manifold’s Riemannian metric gives rise to a unique differential form known as the Riemannian volume form $d\mu$, which allows for the integration of continuous, compactly supported, real-valued functions h over the Riemannian manifold [50]:

$$\int_{\mathcal{M}} h d\mu. \tag{10}$$

Probability Let $\{x_i\}$ be observed samples drawn from P^* , a probability measure supported on \mathcal{M} . Since \mathcal{M} has a lower intrinsic dimension than \mathbb{R}^n , it is “infinitely thin.” In other words, $P^*(\mathcal{M}) = 1$ while the (Lebesgue) volume of \mathcal{M} is 0, meaning no probability density integrated over the ambient space can be used to represent P^* . Formally stated, P^* is not absolutely continuous with respect to the Lebesgue measure on \mathbb{R}^n .

Instead, we require a new way to define the volumes of subsets of \mathcal{M} . We can then formally define a probability density p^* over \mathcal{M} and integrate with respect to this volume to obtain probabilities. The volume form $d\mu$ on \mathcal{M} is the answer; the probability of a set $S \subseteq \mathcal{M}$ can be computed as follows:

$$P^*(S) = \int_S p^* d\mu. \tag{11}$$

We note that the volume form $d\mu$ from differential geometry is not technically a measure in the sense of measure theory. This obstacle is minor: $d\mu$ can be extended to a true measure by a common measure-theoretic tool known as the Riesz-Markov-Kakutani representation theorem⁷ [75]. Thus we may identify $d\mu$ with a measure μ on \mathcal{M} which produces volumes of Borel sets in \mathcal{M} and which we call the Riemannian measure of \mathcal{M} [65].

Formally, we require P^* to be absolutely continuous with respect to μ , and we thus write that p^* is the Radon-Nikodym derivative of P^* with respect to μ : $p^* = \frac{dP^*}{d\mu}$. This is the ground-truth density function we seek to model in this work.

A.2 Experiment details

For all experiments, we use feedforward networks with SiLU activations [37, 68]. All models are trained with the Adam optimizer with the default PyTorch parameters, except for the learning rate which is set as described below [45]. All EBMs, constrained EBMs, and pushforward EBMs are trained with a buffer size of 1000, from which we initialize each Langevin dynamics sample with 95% probability. We do not use spectral normalization for EBMs: we found it harmed the quality of density estimates. Initial noise for the constrained EBM is sampled uniformly from a box in ambient space containing the ground truth manifold and then projected to the manifold by solving for $\operatorname{argmin}_{x_{\text{noise}}} \|F_{\theta}(x_{\text{noise}})\|^2$ with L-BFGS using strong Wolfe line search. Equation 9 is also optimized using a single step of L-BFGS with strong Wolfe line search.

To plot the constrained EBM densities, we estimate the normalizing constants using Monte Carlo. Since the learned MDFs always provide very good approximations of the true manifolds, we estimate each normalizing constant using uniform samples from the *ground truth* manifold for convenience. To plot the pushforward EBM densities, we estimate the normalizing constants in latent space with

⁷In the reference and sometimes in general, this theorem is called the Riesz representation theorem, which can also refer to a different theorem about Hilbert spaces.

Monte Carlo estimates based on uniform sampling within the clamped bounds. We then compute pushforward densities with Equation 2.

All experiments were performed on an Intel Xeon Silver 4114 CPU.

A.2.1 Synthetic data

Motivating Example (Figures 1 and 2) We sampled 1000 points from a von Mises distribution on a unit circle centred at $(0, 0)$ with the mode located at $(1, 0)$ and a concentration of 2.

The MDF for the constrained EBM consisted of 3 hidden layers with 8 units per hidden layer. The MDF was trained for 100 epochs with a batch size of 100, a learning rate of 0.01, $\eta = 1$, and $\alpha = 1$.

The energy function for the constrained EBM consisted of 2 hidden layers with 32 units per hidden layer. It was trained for 40 epochs with a batch size of 100, a learning rate of 0.01, gradients clipped to a norm of 1, and energy magnitudes regularized with a coefficient of 0.1. Langevin dynamics at each training step were run for 10 steps with $\varepsilon = 0.3$, a step size of 1, and energy gradients clamped to maximum values of 0.1 at each step.

The pushforward EBM’s encoder and decoder each had 3 hidden layers with 32 units per hidden layer. They were jointly trained for 300 epochs with a batch size of 100, a learning rate of 0.001, and gradients clipped to a norm of 1.

The pushforward EBM’s energy function had 3 hidden layers and 32 units per hidden layer. It was trained for 200 epochs with a batch size of 100, a learning rate of 0.01, gradients clipped to a norm of 1, and energy magnitudes regularized with a coefficient of 0.1. Langevin dynamics at each training step were run for 60 steps with $\varepsilon = 0.5$, a step size of 10, and energy gradients clamped to maximum values of 0.03 at each step.

Density estimation We sampled 1000 points from a balanced mixture of two von Mises distributions with concentration 2 on circles of unit radius. Respectively, they are centred at $(-2, 0)$ and $(2, 0)$ with modes at $(-1, 0)$ and $(1, 0)$ (or, at polar angles of 0 and π with respect to the centre of each circle).

The MDF for the constrained EBM consisted of 3 hidden layers with 8 units per hidden layer. The MDF was trained for 1000 epochs with a batch size of 100, a learning rate of 0.01, $\eta = 1$, and $\alpha = 1$.

The energy function for the constrained EBM consisted of 3 hidden layers with 32 units per hidden layer. It was trained for 50 epochs with a batch size of 100, a learning rate of 0.01, gradients clipped to a norm of 1, and energy magnitudes regularized with a coefficient of 0.3. Langevin dynamics at each training step were run for 10 steps with $\varepsilon = 0.4$, a step size of 1, and energy gradients clamped to maximum values of 0.1 at each step.

The (ambient) EBM consisted of 2 hidden layers with 32 units per hidden layer (we found that using only 2 hidden layers gave a smoother density). It was trained for 3 cycles of 40 epochs with step sizes of ε^2 , 5, and 10 respectively. We used a batch size of 100, a learning rate of 0.01, gradients clipped to a norm of 1, and energy magnitudes regularized with a coefficient of 0.3. Langevin dynamics at each training step were run for 10 steps with $\varepsilon = 0.005$ and energy gradients clamped to maximum values of 0.03 at each step.

The pushforward EBM’s encoder and decoder each had 3 hidden layers with 32 units per hidden layer. They were jointly trained using a variational autoencoding loss with KL term reweighted with a coefficient of 0.01 for 100 epochs with a batch size of 100, a learning rate of 0.001, and gradients clipped to a norm of 1. We note that the results appeared very similar when trained without the KL term at all (i.e. as an autoencoder).

The pushforward EBM’s energy function had 3 hidden layers and 32 units per hidden layer. It was trained for 100 epochs with a batch size of 100, a learning rate of 0.01, gradients clipped to a norm of 1, and energy magnitudes regularized with a coefficient of 0.1. Langevin dynamics at each training step were run for 60 steps with $\varepsilon = 0.5$, a step size of 10, and energy gradients clamped to maximum values of 0.03 at each step.

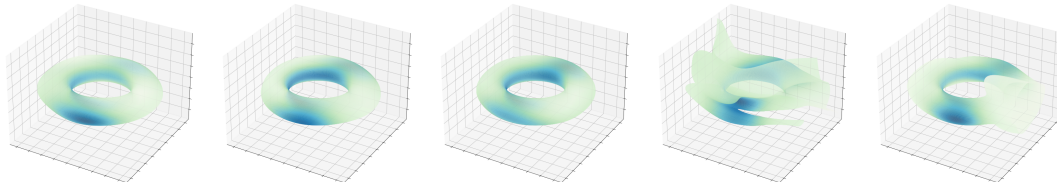


Figure 8: Constrained EBM manifold learning and density estimation results on the glycine angle data for different values of η , the hyperparameter setting the boundary under which singular values will be penalized by the Jacobian regularization term. From left to right: $\eta = 0.3$, $\eta = 1$, $\eta = 2$, $\eta = 3$, and $\eta = 5$.

Manifold arithmetic We sampled 1000 points from a balanced mixture of two projected normal distributions on the unit sphere. Each component was a normal distribution with unit diagonal covariance centred at $(1, 0, 0)$ and $(-1, 0, 0)$ respectively before being projected to the sphere.

The MDF for the constrained EBM consisted of 3 hidden layers with 8 units per hidden layer. The MDF was trained for 1500 epochs with a batch size of 100, a learning rate of 0.01, $\eta = 1$, and $\alpha = 2$.

The energy function for the constrained EBM consisted of 2 hidden layers with 32 units per hidden layer. It was trained for 5 rounds of 10 epochs each wherein Langevin dynamics was run for 5, 10, 20, 40, and 50 steps respectively. We used a batch size of 50, a learning rate of 0.01, gradients clipped to a norm of 1, and energy magnitudes regularized with a coefficient of 1. Langevin dynamics at each training step were run for 10 steps with $\varepsilon = 0.1$, a step size of ε^2 , and energy gradients clamped to maximum values of 0.03 at each step.

A.2.2 Natural data

Geospatial data The MDF for the constrained EBM consisted of 3 hidden layers with 8 units per hidden layer. The MDF was trained for 500 epochs with a batch size of 100, a learning rate of 0.01, $\eta = 1$, and $\alpha = 2$.

The energy function for the constrained EBM consisted of 4 hidden layers with 32 units per hidden layer. It was trained for 4 rounds of 10 epochs each wherein Langevin dynamics was run for 5, 10, 20, and 40 steps respectively. We used a batch size of 100, a learning rate of 0.01, gradients clipped to a norm of 1, and energy magnitudes regularized with a coefficient of 1. Langevin dynamics at each training step was run with $\varepsilon = 0.1$, a step size of ε^2 , and energy gradients clamped to maximum values of 0.03 at each step.

The pushforward EBM’s encoder and decoder each had 4 hidden layers with 32 units per hidden layer. They were jointly trained for 500 epochs with a batch size of 100, a learning rate of 0.001, and gradients clipped to a norm of 1.

The pushforward EBM’s energy function had 4 hidden layers and 32 units per hidden layer. It was trained for 50 epochs with a batch size of 100, a learning rate of 0.01, gradients clipped to a norm of 1, and energy magnitudes regularized with a coefficient of 0.1. Langevin dynamics at each training step were run for 60 steps with $\varepsilon = 0.5$, a step size of 10, and energy gradients clamped to maximum values of 0.03 at each step.

Amino acid modelling The MDF for the constrained EBM consisted of 2 hidden layers with 8 units per hidden layer. The MDF was trained for 500 epochs with a batch size of 100, a learning rate of 0.01, $\eta = 0.3$, and $\alpha = 1$. We found that increasing η , the smallest singular value required of J_{F_θ} by the regularization term, made the implicit manifold harder to optimize. This occasionally yielded plateaus in the loss function and resulted in incorrect manifolds, depicted in Figure 8.

The energy function for the constrained EBM consisted of 2 hidden layers with 32 units per hidden layer. It was trained for 2 rounds of 10 epochs each wherein Langevin dynamics was run for 5 and 10 steps respectively. We used a batch size of 100, a learning rate of 0.01, gradients clipped to a norm of 1, and energy magnitudes regularized with a coefficient of 1. Langevin dynamics at each training step was run for 10 steps with $\varepsilon = 0.1$, a step size of ε^2 , and energy gradients clamped to maximum values of 0.03 at each step.

The pushforward EBM's encoder and decoder each had 4 hidden layers with 32 units per hidden layer. They were jointly trained for 500 epochs with a batch size of 100, a learning rate of 0.001, and gradients clipped to a norm of 1.

The pushforward EBM's energy function had 3 hidden layers and 32 units per hidden layer. It was trained for 50 epochs with a batch size of 100, a learning rate of 0.01, gradients clipped to a norm of 1, and energy magnitudes regularized with a coefficient of 0.1. Langevin dynamics at each training step were run for 60 steps with $\varepsilon = 0.5$, a step size of 10, and energy gradients clamped to maximum values of 0.03 at each step.